Modeling self-ignition of high-pressure hydrogen leaks in confined space

Marc Le Boursicaud, Song Zhao, Jean-Louis Consalvi, Pierre Boivin

Modeling self-ignition of high-pressure hydrogen leaks in confined space

Marc Le Boursicaud[a,*], Song Zhao[a], Jean-Louis Consalvi[b], Pierre Boivin[a]

[a] *Aix Marseille Univ, CNRS, Centrale Med, M2P2, Marseille, France*
[b] *Aix Marseille Univ, CNRS, IUSTI, Marseille, France*

Abstract

The numerical study of ignition risk in the event of high-pressure hydrogen leakage presents numerous challenges. The first is to properly simulate the complex multi-dimensional flow, characterized by a hemispherical expanding shock and a contact discontinuity. The second is to accurately resolve the diffusion/reaction interface, which exhibits a very small length scale compared to the jet radius. These challenges were addressed in our previous work (Le Boursicaud *et al.*, Combust. Flame 274, 2025), leading to the development of a reduced-order model capable of efficiently predicting the risk of self-ignition in the case of high-pressure hydrogen storage leakage for various geometries.

The present work focuses on extending the previously developed model to account for the effects of leakage in confined spaces. These modifications include a simple adjustment of the pseudo-1D model to account for shock reflection, as well as the consideration of entropy jumps occurring during the interaction between the reflected shock wave and the diffusion layer. This work is motivated by the potential increase in ignition risk when leaks occur in confined environments, as opposed to the open environments previously considered (Smygalina and Kiverin, Int. J. Hydrog. Energy 47, 2022).

Novelty and Significance Statement: This work extends a reduced-order model for shock-induced ignition of high-pressure hydrogen leaks from open to confined environments, capturing key effects such as shock reflection and shock–contact interaction. It enables efficient assessment of ignition risk in scenarios where full-resolution simulations are computationally prohibitive.

*Corresponding author.
Email address: marc.leboursicaud@gmail.com (Marc Le Boursicaud)

Authors Contributions Statement:
-M.LB. : Designed research, Software, Formal analysis, Writing - original draft
-S.Z. : Supervision, Writing - review & editing
-JL.C. : Supervision, Writing - review & editing
-P.B. : Supervision, Funding acquisition, Writing - review & editing

Keywords: Shock-induced ignition, Reduced-order model, Leakage, Hydrogen safety

---

1. Introduction

1.1. Problem description

The increasing use of hydrogen as a carbon-free fuel in the transportation and industrial sectors raises significant safety concerns. While canonical hydrogen ignition scenarios are now well understood [1], there remains a gap in understanding and developing appropriate tools for more complex configurations representative of emerging hydrogen applications—particularly high-pressure storage. Our previous work [2] focused on developing an efficient methodology to study the self-ignition of high-pressure hydrogen leakage into ambient air. This approach, inspired by the work of Maxwell and Radulescu [3], was specifically tailored to leakage scenarios in open environments. It enabled the efficient determination of the ignition limit—i.e., the boundary in terms of leakage radius (denoted r) and storage pressure (denoted $p_{\mathrm{H_2},0}$ or p_{storage})—for several geometries.

The present study aims to extend this methodology to address the critical problem of leakage in confined environments, representative of engine casings or simply a wall located near the failure point. This issue is of particular relevance to hydrogen safety, as highlighted in both experimental [4–6] and numerical [7, 8] studies, which showed that the presence of an obstacle in front of the leakage can promote shock-induced ignition due to the reflected shock wave.

This study focuses on the increased ignition risk caused by the presence of an infinitely long flat obstacle placed in front of the leakage, as numerically investigated by Smygalina and Kiverin [7]. They studied the influence of such an obstacle on the ignition limits in both two-dimensional and three-dimensional leakage configurations from tanks and pipes. Their results confirmed that the obstacle can significantly reduce the pressure required to reach the ignition limit, with a strong dependence on the leakage geometry (e.g., 2D or 3D, tank or pipe).

However, Ref. [7] employed a classical DNS-like approach to model both the flow and the diffusion layer within a single simulation, without applying dedicated grid refinement techniques. As shown in our previous study, accurately resolving the diffusion layer where ignition occurs requires an extremely fine mesh, which comes with a substantial computational cost. To the author's knowledge, no efficient framework or strategy has yet been employed to numerically assess the effect of obstacles on the ignition risk associated with high-pressure hydrogen release, which serves as the motivation for the present study.

1.2. Leakage in confined-space problem description

The problem considered in the previous study is similar to that presented in [2, 3], with the addition of a wall placed in front of the leakage at a distance L, as illustrated in the sketch on the left of Fig. 1. This figure shows the anticipated evolution of the leading shock wave (shown in red) and the hydrogen plume (shown in gray) at three distinct times.

The sketch on the left represents the scenario prior to the reflection of the leading shock wave. The middle sketch illustrates the system's evolution following the reflection of the shock wave off the wall, generating a reflected shock wave shown in blue. Finally, the sketch on the right depicts the interaction between the reflected shock wave and the contact discontinuity. The times associated with these two events are denoted as t_R for the shock reflection and t_{SC} for the shock-contact interaction.

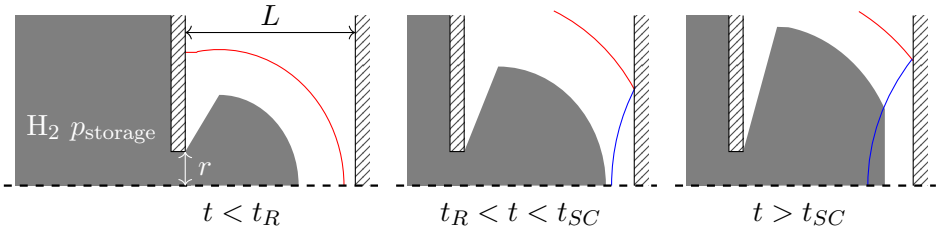

Figure 1: Sketch of a high-pressure tank leakage in a confined space.

From a phenomenological perspective, the reflection of the leading shock wave is expected to produce a stronger reflected wave, resulting in elevated pressure and temperature in the post-shock region. As the reflected shock wave propagates backward, it interacts with the diffusion layer, which corresponds to the contact discontinuity from a flow dynamics perspective. This interaction primarily leads to an increase in temperature and pressure within the diffusion layer.

Figure 2 illustrates the temperature and pressure fields for a two-dimensional leakage from a tank at an initial hydrogen pressure of $p_{H_2,0} = 300$ atm, depicting the conditions before the shock reflection (on the left) and after the shock-contact interaction (on the right). In addition, the leading, secondary and reflected shock waves are indicated, as well as the contact discontinuity.

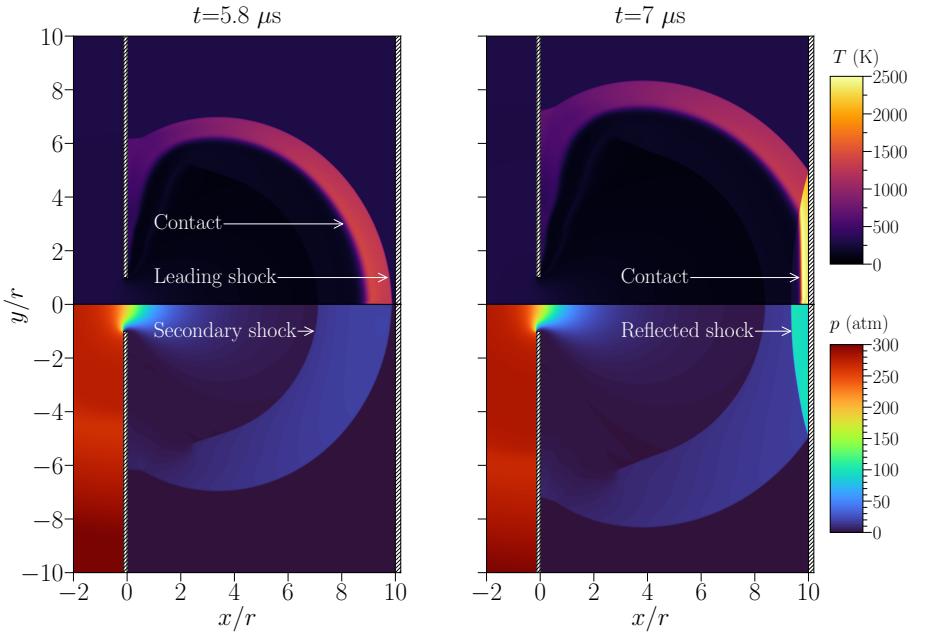

Figure 2: Temperature (top), pressure (bottom) fields obtained with ECOGEN [9] for a hydrogen tank pressure of $p_{H_2,0} = 300$ atm and a leakage radius of r=1 mm before the leading shock wave reflection at a time $t = 5.8$ μs ($< t_R$, left), and after at a time t=7.0 μs ($> t_{SC}$, right).

The increase in pressure and temperature accelerates the ignition process, leading to ignition in cases where it would otherwise be inhibited in an open-space configuration. Additionally, the farther the obstacle is from the leakage, the weaker the reflected shock will be. This means that the parameter L is now as important as the hydrogen storage pressure, noted $p_{H_2,0}$ or p_{storage} and the leakage size r in determining the ignition limits.

1.3. Previous approach and notation

The novel approach proposed in the previous study is based on scale separation. As the diffusion/reaction layer is several orders of magnitude smaller than the characteristic length of the flow, it can be solved as a separate problem, requiring only the proper initial conditions and the evolution

of the pressure within the layer. This pressure evolution was simply modeled by a power law for a 3D tank leakage in Ref. [3]. However, the previous study proposed a more general pseudo-1D model to simulate at low cost the dynamics of the flow along the centerline, where ignition is most likely to occur. This was achieved by blending 1D and 2D/3D formulations using planar, cylindrical, and spherical coordinates in a single framework. The resulting set of equations to be solved for the flow are:

$$\frac{\partial \rho}{\partial t} + \frac{\partial \rho u}{\partial x} = -\mathcal{S}(x,t)\rho u \tag{1}$$

$$\frac{\partial \rho u}{\partial t} + \frac{\partial \rho u u + p}{\partial x} = -\mathcal{S}(x,t)\rho u u \tag{2}$$

$$\frac{\partial \rho e_t}{\partial t} + \frac{\partial \rho u e_t + p u}{\partial x} = -\mathcal{S}(x,t)\left(\rho u e_t + p u\right) \tag{3}$$

$$\frac{\partial \rho Y_{\mathrm{H_2}}}{\partial t} + \frac{\partial \rho u Y_{\mathrm{H_2}}}{\partial x} = -\mathcal{S}(x,t)\rho u Y_{\mathrm{H_2}} \tag{4}$$

where e_t is the total energy per unit mass, $Y_{\mathrm{H_2}}$ is the hydrogen mass fraction (as only two species needs to be considered for the flow: hydrogen and air), and $\mathcal{S}$ is the source term, illustrated for the tank or pipe configuration in Fig. 3 and are given by:

$$\mathcal{S}_{\mathrm{tank}}(x,t) = \begin{cases} 0 & \text{if } t < t_E \\ \frac{\alpha}{r}\frac{6\chi^3-9\chi^2+38\chi-18}{6\chi^4-12\chi^3+39\chi^2-17\chi+33} & \text{otherwise} \end{cases} \tag{5}$$

$$\mathcal{S}_{\mathrm{pipe}}(x,t) = \begin{cases} 0 & \text{if } t < t_E \text{ or } x < 0 \\ \frac{\alpha}{r}\frac{13\chi^2+8\chi}{13\chi^3+4\chi+51} & \text{otherwise} \end{cases} \tag{6}$$

In Eqs. (5) and (6), α is a parameter representing the dimension of the problem (2D: α=1, 3D: α=2), χ is the dimensionless space coordinate given by $\chi = x/r$. Finally, t_E denoted the time at which the flow on the centerline can no longer be consider purely 1D, using the speed of sound (noted c) computed from the solution of the initial Riemann problem on both sides of the contact (denoted by "$\mathrm{H_2}, L$" and "air, R"):

$$t_E = \min\left(r/c_{\mathrm{H_2},L}, r/c_{\mathrm{air},R}\right). \tag{7}$$

Once the flow is simulated and the evolution over time of the pressure at the contact discontinuity is obtained (the entire diffusion layer is point-like and corresponds to the contact from the flow perspective), the reactive

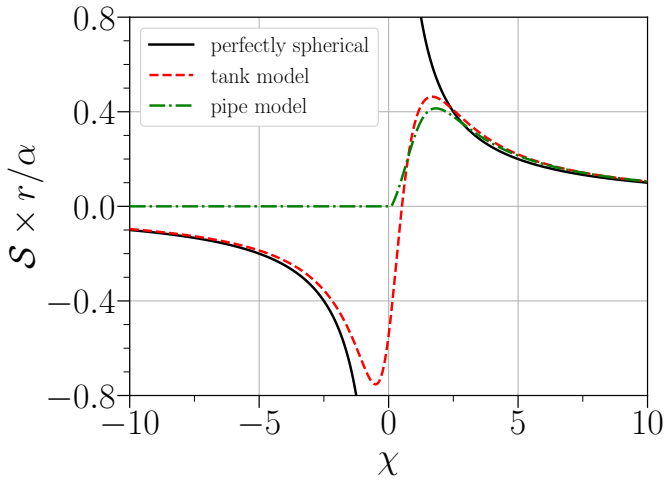

Figure 3: Source term profile for the tank geometry (dashed red curve) and the pipe geometry (green shad-dotted curve) compared to the source term for perfectly spherical flow (black solid curve)

diffusion layer can be simulated to determine whether ignition occurs. As the velocity and pressure are uniform across a contact discontinuity (and thus within the entire diffusion layer), only the mass fraction and temperature equations need to be solved. A Lagrangian approach is used, together with a mass-weighted coordinate variable, noted m, defined as:

$$m = \int_0^x \rho(x,t)dx \tag{8}$$

to keep a compact mesh (as the diffusion layer thickens over time). Finally, a previously proposed passive scalar approach is used to further simplify the solution of the diffusion layer problem without compromising accuracy. This model consists of solving only the diffusion of the main species (hydrogen and air), while the ignition process is represented by an additional, self-reacting scalar, noted η. This scalar is only weakly coupled to the main species and temperature equations, meaning it is not considered in the mass conservation, equation of state, or energy equation. More details about the passive scalar approach can be found in [10]. The resulting equations to be solved for the diffusion layer are:

$$\rho\frac{\partial Y_{\mathrm{H_2}}}{\partial t} = \rho\frac{\partial}{\partial m}\left(\rho^2 D_{\mathrm{H_2}}\frac{W_{\mathrm{H_2}}}{W}\frac{\partial X_{\mathrm{H_2}}}{\partial m}\right) \tag{9}$$

$$\rho c_p \frac{\partial T}{\partial t} = \frac{\mathrm{D}p}{\mathrm{D}t} + \rho \frac{\partial}{\partial m}\left(\rho\kappa \frac{\partial T}{\partial m}\right) + \rho^3 (c_{p,\mathrm{H_2}} - c_{p,\mathrm{air}}) D_{\mathrm{H_2}} \frac{\partial T}{\partial m}\frac{\partial Y_{\mathrm{H_2}}}{\partial m} \tag{10}$$

$$\rho \frac{\partial Y_\eta}{\partial t} = \omega_\eta + \rho \frac{\partial}{\partial m}\left(\rho^2 D_\eta \frac{W_\eta}{W}\frac{\partial X_\eta}{\partial m}\right) \tag{11}$$

where D_k are the diffusion coefficients, κ is the thermal conductivity, and $\frac{\mathrm{D}p}{\mathrm{D}t}$ is the pressure evolution term obtained from the flow simulation.

In addition, dimensionless variables need to be introduced. The first is the space coordinate χ, introduced above, which leads to the definition of the obstacle's dimensionless position, $\chi_L = L/r$.

The second is the dimensionless time variable, introduced in the work of Maxwell and Radulescu [3], and defined as:

$$\tau = t\left(\frac{\rho_{\mathrm{air},0}}{\rho_{\mathrm{H_2},0}}\left(\frac{2}{\gamma_{\mathrm{H_2},0}+1}\right)^{-1/(\gamma_{\mathrm{H_2},0}+1)}\right)^{1/2} \frac{c_{\mathrm{H_2},0}}{1.2r}\left(\frac{2}{\gamma_{\mathrm{H_2},0}+1}\right)^{1/2} \tag{12}$$

where c and γ denote the speed of sound and the heat capacity ratio, respectively, and the subscript "0" refers to the initial hydrogen or ambient air conditions.

More details about the approach can be found in the original reference [2].

1.4. Proposed methodology

Before proceeding with the necessary adjustments to the methodology, it is important to note that the shock-contact interaction is a non-isentropic process due to the presence of the reflected shock wave. Consequently, the pressure evolution alone cannot reliably predict the post-interaction state within the diffusion framework. At the time of the shock-contact interaction, the diffusion layer fields must be updated using the entropy jumps on both the hydrogen and air sides. These entropy jumps must be computed based on the fields provided by the flow solver. However, the numerical methods employed in the flow solver do not produce sharp discontinuities. This limitation is particularly pronounced for the contact discontinuity, as the solver uses a diffused interface approach, requiring the discontinuity to be spread across several cells for numerical stability. As a result, the entropy jumps cannot be directly obtained from a simple before-and-after reading of the flow fields around the contact. The detailed method used to address this challenge will be discussed in a dedicated section.

In summary, three major modifications to the methodology are required:

- Modification of the flow solver to predict the evolution following the shock reflection, at least up to the shock-contact interaction.
- Evaluation of the entropy jumps for both the hydrogen and air sides of the contact, based on the fields provided by the flow solver.
- Adjustment of the diffusion framework to incorporate entropy jumps instead of solely relying on the pressure jump.

These changes will be addressed in their respective sections, followed by a presentation of the main results and conclusions.

2. Modification of the pseudo-1D solver

The first modification to the pseudo-1D code to account for confined leakage involves implementing a wall boundary condition. This addition is standard and does not raise any difficulty. The main difficulty, however, lies in the shape of the reflected shock wave. Indeed, it is important to note that, with the approach adopted here, the shape of the reflected shock wave (e.g., concentric in the case of a perfectly spherical geometry) does not depend on the boundary condition itself but rather on the treatment of the source term. As highlighted in the previous study, the source term defines the type of symmetry that the flow is constrained to follow.

2.1. Modification of the source term

With this consideration in mind, the simple approach adopted here, assumes that the reflected shock wave can be regarded as the mirror image of the leading shock wave that would have been obtained in the absence of the obstacle. This concept is illustrated in the sketch shown in Fig. 4 with the leading shock wave (in red), reflected one (in blue) and their mirrored images produced by the obstacle (dashed curves).

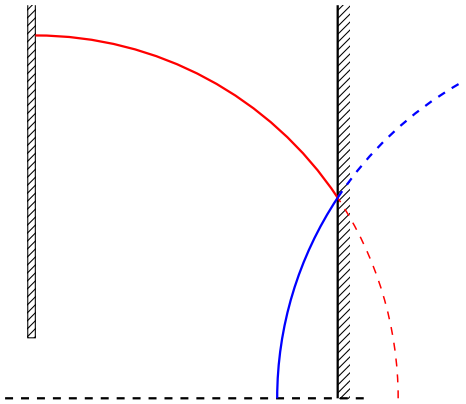

Figure 4: Sketch of the reflection (blue) of the leading shock wave (red) and their image mirrored by the obstacle (dashed curves).

This leads to the definition of χ^*, the mirrored dimensionless coordinate:

$$\chi^* = \frac{2L - x}{r} = 2\chi_L - \chi. \tag{13}$$

Using this definition, the radius of the reflected shock wave at a position χ_{shock} corresponds to the radius of the shock wave at a position $\chi^*_{\text{shock}}{=}2\chi_L{-}\chi_{\text{shock}}$ in the absence of the obstacle. Therefore, the source term within the domain bounded by the reflected shock wave and the obstacle can be computed as $\mathcal{S}(\chi){=}{-}\mathcal{S}(\chi^*)$. Note that the sign of the source term is inverted because the reflected shock wave travels in the opposite direction of the leading shock wave, resulting in an oriented curvature with an opposite sign. This consideration leads to the updated formulation of the tank and pipe source term models [2]:

$$\mathcal{S}_{\text{tank}}(x,t) = \begin{cases} 0, & \text{if } t < t_E \\ \frac{\alpha}{r}\frac{6\chi^3-9\chi^2+38\chi-18}{6\chi^4-12\chi^3+39\chi^2-17\chi+33}, & \text{if } t < t_R \text{ or } \chi < \chi_{\text{shock}} \\ -\frac{\alpha}{r}\frac{6{\chi^*}^3-9{\chi^*}^2+38\chi^*-18}{6{\chi^*}^4-12{\chi^*}^3+39{\chi^*}^2-17\chi^*+33}, & \text{otherwise} \end{cases} \tag{14}$$

$$\mathcal{S}_{\text{pipe}}(x,t) = \begin{cases} 0, & \text{if } t < t_E \text{ or } \chi < 0 \\ \frac{\alpha}{r}\frac{13\chi^2+8\chi}{13\chi^3+4\chi+51}, & \text{if } t < t_R \text{ or } \chi < \chi_{\text{shock}} \\ -\frac{\alpha}{r}\frac{13{\chi^*}^2+8\chi^*}{13{\chi^*}^3+4\chi^*+51}, & \text{otherwise} \end{cases} \tag{15}$$

The source term derived from Eq. (14) for an obstacle position at $\chi_L{=}10$ is illustrated in Fig. 5 before the shock reflection and for two positions after the shock reflection.

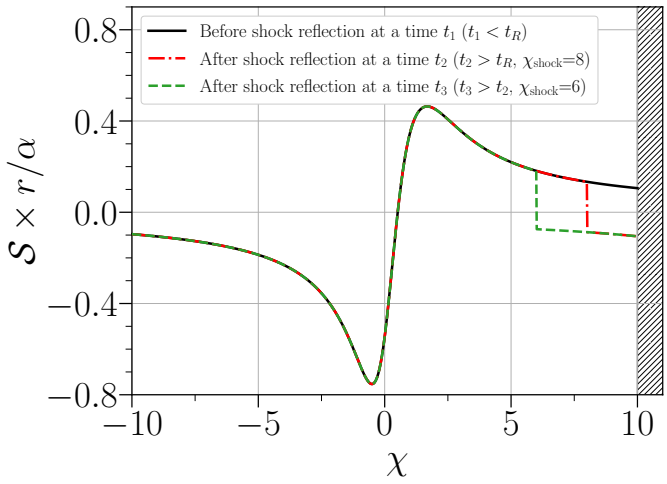

Figure 5: Comparison of the dimensionless source term coefficients profiles $\mathcal{S}$ for a wall placed at χ_L=10, before the leading shock wave is reflected at a time t_1 ($< t_R$, black curve), after the reflection at a time t_2 ($> t_R$, red dashed curve) and later at a time t_3 ($> t_2$, green dashed curve).

2.2. Validation of the new source term model

Two cases were simulated to validate the new source term model: one for a 2D tank at $p_{\text{H}_2,0} = 300$ atm, and another for a 2D pipe at $p_{\text{H}_2,0} = 100$ atm. These simulations were performed,on the one hand, with ECOGEN [9] used as a reference and, on the other hand, with the updated pseudo-1D solver employing Eq. (14) and Eq. (15). Both cases feature a leakage size of r =1.0 mm and an obstacle positioned at L =20 mm. A grid size Δx=$r/50$ and a CFL=0.8 were used for both ECOGEN and the pseudo-1D solver (as a reminder both solver uses the HLLC approximate Riemann solver). The resulting x-t diagrams, based on the leading shock wave (which becomes the reflected shock), the contact discontinuity, and the secondary shock (or Mach shock), are shown in Fig. 6.

An overall excellent agreement is observed for both cases up to the shock-contact interaction. After this point, however, the reflected shock wave trajectories predicted by the pseudo-1D solver begin to diverge from those obtained in the ECOGEN simulations. This divergence is expected because the reflected shock wave is altered by the shock-contact interaction. The phenomenon can be easily understood: the contact discontinuity represents a sharp change in composition, temperature and therefore speed of sound. In analogy to light refraction, the shock wave passing through the contact experiences a change in both its speed and shape. The deformation of the

shock front no longer corresponding to the mirror image used for the model as described in Sec. 2.1. This altered shock will be referred to as the transmitted shock throughout this article. This scattering-like phenomenon is further illustrated in Fig. 7 that shows the density field of the previously described pipe case after the shock-contact interaction. It is evident that the transmitted shock differs in shape from the incident (reflected) one.

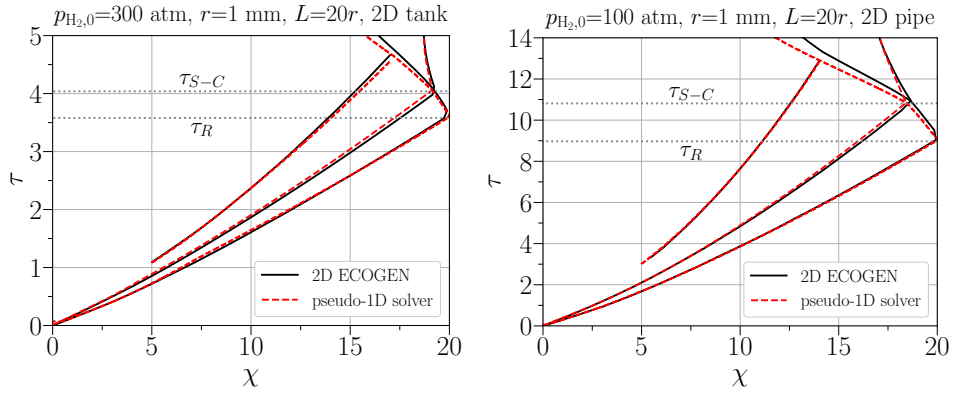

Figure 6: Comparison of the x-t diagram of the main shock wave, the contact discontinuity and the secondary shock, obtained from a simulation with ECOGEN (black curves) and with the present modified pseudo-1D model (red dashed curves). The leakage size is fixed at $r = 1.0$ mm, and the obstacle placed at a distance $\chi_L = 20$, with a tank pressure of $p_{H_2,0} = 300$ atm on the right and a pipe pressure of $p_{H_2,0} = 100$ atm on the left.

The comparison of the pressure at the contact is reported in Fig. 8. The agreement between the two simulations is still excellent up to the interaction. After this point, the pressures begin to diverge. Notably, the fact that the pressure decreases again after the interaction is consistent with the two-dimensional simulation obtained using ECOGEN. However, it is important to highlight that the peak pressure following the shock-contact interaction is approximately the same in both simulations. The primary discrepancy lies in the pressure decay, which is underestimated by the present pseudo-1D model after the interaction. As a result, the model overestimates the pressure and, consequently, the reactivity within the diffusion layer only after this event. This overestimation of reactivity leads to more conservative ignition limits from a safety perspective.

The pseudo-1D solver has been extended and is now able to predict the flow behavior after shock reflection. The next step will focus on the shock-contact interaction to predict the entropy jumps.

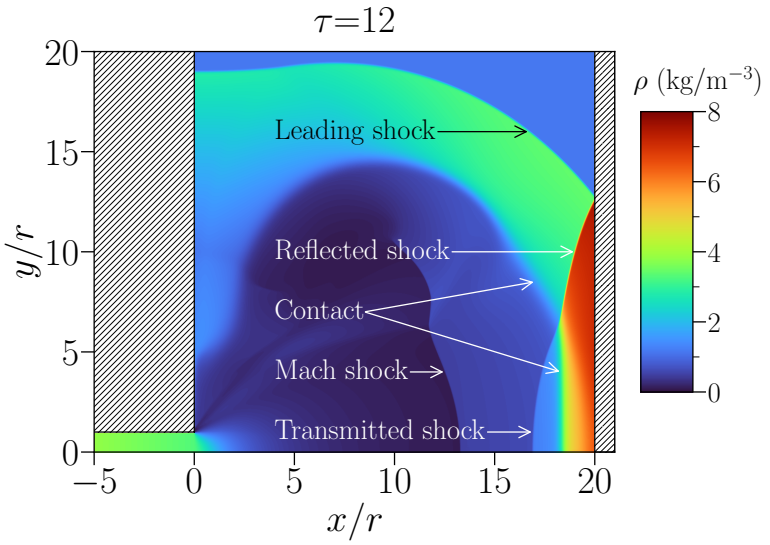

Figure 7: Density field obtained with ECOGEN [9] after the shock-contact interaction at a time τ=12 (t=25 μs > t_{SC}) for a hydrogen pipe at $p_{H_2,0}$=100 atm, a two-dimensional leakage with a radius of r=1 mm and an obstacle placed at χ_L=20.

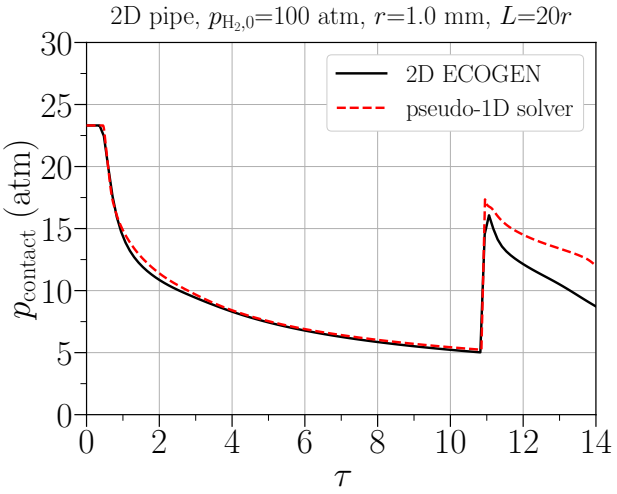

Figure 8: Evolution with time of the pressure at the contact obtained from a simulation with ECOGEN [9] (black curve) and with the pseudo-1D flow model (red dashed curve) for a hydrogen pipe at $p_{H_2,0}$=100 atm, a two-dimensional leakage with a radius of r=1 mm and an obstacle placed at χ_L=20.

3. Taking into account the shock-contact interaction

3.1. Interaction as a Riemann problem

From the centerline perspective, the shock-contact interaction can be viewed as a Riemann (or shock tube) problem (with non-zero initial velocities) since the interaction is, in theory, punctual and infinitely fast. This interaction is expected to produce a transmitted shock wave, traveling in the same direction as the incident shock, a contact discontinuity (with both sides' fields altered compared to the initial contact), and rarefaction waves propagating in the opposite direction of the shock. This is analogous to light reflection and transmission, with a scattering-like effect in multidimensional cases, as mentioned previously. Figure 9 shows a sketch of the waves and the nomenclature used. The left (hydrogen) and right (air) sides of the contact will be denoted as L and R, with the indices 1 and 2 referring to the pre- and post-interaction states, respectively. Furthermore, the state behind the incident shock (reflected) is denoted as S_1. The state behind the transmitted shock will be denoted as S_2 in this nomenclature, which also corresponds to the state L_2. The latter notation is retained.

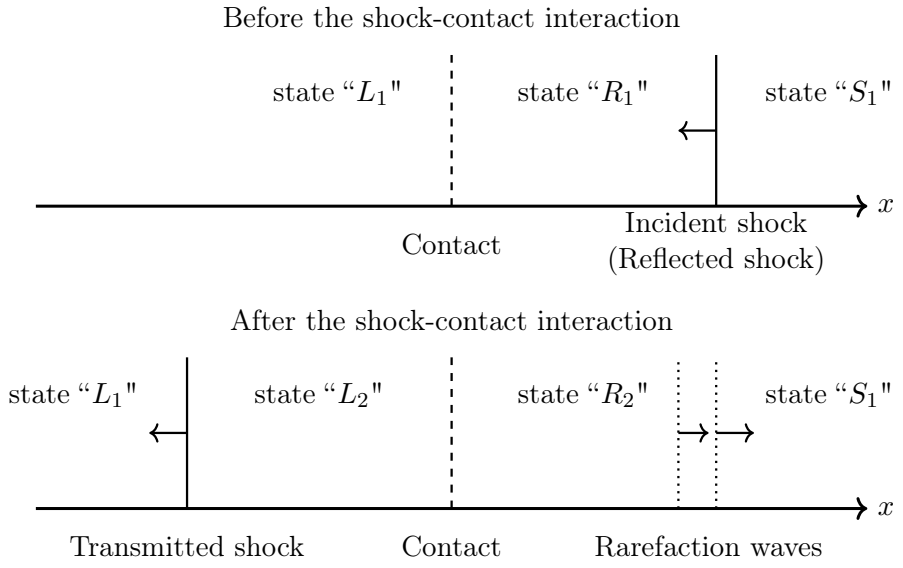

Figure 9: Sketch of the interaction between the contact and the reflected shock wave.

The entropy jumps that need to be recovered are Δs_L and Δs_R, defined as:

$$\Delta s_L = s(L_2) - s(L_1) \tag{16}$$
$$\Delta s_R = s(R_2) - s(R_1) \tag{17}$$

with s the specific entropy.

The difficulty in evaluating these two entropy jumps arises from the thickening of the waves due to numerical methods as well as the continuous evolution of the flow in our case. Therefore, it is impossible to directly evaluate the states R_1, R_2, and L_2, as they are all contained between different waves and are strongly affected by numerical thickening. It may be possible to estimate them at a later time, once the transmitted shock and rarefaction tail have moved far enough from the contact; however, this would not correspond to the post-interaction values since the flow remains unsteady. In contrast, the states L_1 and S_1 can be estimated from the pseudo-1D flow, but only with careful extrapolation, which will be detailed in the next section. From these two states, it will be possible to construct and solve the Riemann problem (corresponding to the interaction) using classical semi-analytical methods.

3.2. States extrapolation

As mentioned, a specific extrapolation is needed to evaluate the states L_1 and S_1 from the pseudo-1D solver fields. The selected approach involves evaluating the primitive variables ρ, u, and p on either side of the interaction using 6 different first-degree polynomials. The relevance of a first-degree polynomial will be justified during the discussion of the test cases. It is important to note that Y_{H_2} does not need to be evaluated, as it is always equal to 1 on the left side and 0 on the right side of the contact discontinuity. The polynomials are fitted based on cells that are sufficiently close to the interaction to be representative of the local flow, yet far enough to avoid the numerically smoothed regions around the waves. It was observed that the polynomials can be constructed from only five cells provided that these cells are at least 15 cells away from the interaction to avoid the numerically thickened regions. Denoting I_{SC} the cell index at the center of the interaction (defined as the center of the contact where Y_{H_2} is the closest to 0.5), the indices of the cells used to fit the polynomials are given in Table 1.

This stencil was found optimal for our numerical schemes, which consist of a MUSCL-Hancock to reconstruct the variable on the cells surfaces, using the van Albada slope limiter for all primitive variables, along with an HLLC solver using the Roe wave speed estimation to compute the fluxes. It is important to note that using a different limiter (such as the Ultrabee [11]) for

Discontinuity at index I_{SC}	Cell index used for the fitting
Left side	$]I_{SC}-20, I_{SC}-15]$
Right side	$[I_{SC}+15, I_{SC}+20[$

Table 1: Cell indices for the polynomial fit.

the different variables would result in less numerically thickened profiles [12], the choice to keep the same cells for all variables suggests using only one limiter for the interpolations. The choice of the stencil is illustrated and validated on simple 1D planar and 1D spherical test cases in Appendix A.

More elegant solutions, such as deconvolution of the fields based on the mass fraction profile (which would eliminate the numerical filtering of the contact), are possible. However, this approach was not chosen for the sake of simplicity.

3.3. Entropy jumps reconstruction

Now that the states L_1 and S_1 have been obtained through extrapolation, the entropy jumps can be computed. The goal is to determine the states just after the interaction (L_2 and R_2). These states are obtained by solving the one-dimensional Riemann problem defined by the states L_1 and R_1. This can be achieved efficiently using classical semi-analytical methods for shock tube problems. The only missing state is R_1, which satisfies the following contact discontinuity relations:

$$u(L_1) = u(R_1) \tag{18}$$
$$p(L_1) = p(R_1). \tag{19}$$

It is therefore possible to reconstruct the last unknown state, $\rho(R_1)$, that satisfies the jump condition across the incident (reflected) shock wave to transition to state S_1. With two unknowns remaining (the density $\rho(R_1)$ and the transmitted shock displacement speed σ), the density and momentum shock relations are used to close the problem:

$$\rho(R_1)\left[u(R_1)-\sigma\right] = \rho(S_1)\left[u(S_1)-\sigma\right] \tag{20}$$
$$\rho(R_1)\left[u(R_1)-\sigma\right]^2 + p(R_1) = \rho(S_1)\left[u(S_1)-\sigma\right]^2 + p(S_1). \tag{21}$$

Combining Eqs. (20) and (21) yields the following expression:

$$\frac{1}{\rho(R_1)} = \frac{1}{\rho(S_1)} - \frac{[u(R_1) - u(S_1)]^2}{p(R_1) - p(S_1)}. \tag{22}$$

To summarize, the entropy jumps are computed from the entropy of the four states, L_1, L_2, R_1, and R_2, as given by Eqs. (16) and (17). The states L_1 and S_1, located on the left and right sides of the discontinuity at the moment of the shock-contact interaction, are obtained using the extrapolation procedure for the primitive variables (i.e. ρ, u, and p). The state R_1 is then computed based on contact discontinuity and shock relationships using Eqs. (18), (19), and (22). Finally, the states L_2 and R_2 are obtained by solving the Riemann or shock tube problem defined by the two states L_1 and R_1. This methodology can be applied to any thermodynamic model that defines how entropy is computed based on the primitive variables. In our particular case, as the NASA 7 polynomials are used, entropy is a function of temperature. Since temperature is obtained from the perfect gas equation of state, the variables ρ, p, and Y_{H_2} are required to compute the entropy.

Figure 10 shows the exact entropy jumps for the hydrogen and air sides, as well as those obtained using the present methodology, in the case of a planar hydrogen/air shock tube with a wall on the air side, as a function of the initial hydrogen pressure.

This method could be used to directly obtain the post-interaction temperature on both sides for the diffusion layer. However, the choice was made to compute the entropy jumps first and then use them within the diffusion framework to determine the correct temperature. This approach was chosen to mitigate the risk of error accumulation during extrapolation. It was considered more prudent to compute the entropy jumps based on the extrapolated values, as they are not exactly the states simulated in the diffusion framework (where both boundary conditions of the diffusion framework should correspond to the L and R states in the flow). This discrepancy arises due to small errors in the extrapolation procedure, as well as in the numerical solving of the flow and the diffusion layer. To maintain consistency between the solvers, the entropy jump formulation was used instead of directly imposing the post-interaction states.

3.4. Modification of the diffusion framework

The final modifications concern the diffusion framework. At the time of the shock-contact interaction, the entropy jumps are used instead of pressure to update the temperatures within the diffusion layer. The two entropy jumps obtained in the previous section represent the jumps observed by the

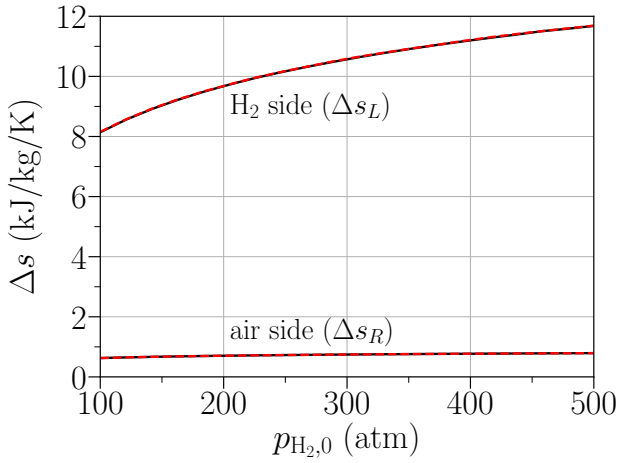

Figure 10: Entropy jumps of the shock-contact interaction in the case of a planar hydrogen/ambient air shock tube problem with a wall on the air side. Analytical solution (black curves) and the one obtained with Eqs. 16 and 17 (red dashed curves) based on the semi-analytical shock-contact interaction computation.

two boundary conditions in the diffusion framework. To update the entire temperature profile, the entropy jumps are applied to all points using a mass-averaging approach as follows:

$$s_2(m) = s_1(m) + Y_{H_2}(m)\Delta s_L + (1 - Y_{H_2}(m))\,\Delta s_R, \tag{23}$$

where s_1 and s_2 are the entropy profiles within the diffusion layer before and after the interaction, respectively.

Once the new entropy profile s_2 is obtained, it is used along with the hydrogen mass fraction to compute the corresponding temperature.

3.5. Validation of the entropy jumps prediction

In order to validate the present method to predict the correct evolution of the variables on both sides of the contact discontinuity (and therefore within the diffusion layer), a spherical shock reflection test case is used. It consists of a shock tube problem in spherical coordinates, with hydrogen at 100 atm at the center and air at atmospheric pressure on the outer side, both initially at 300 K. A circular obstacle (to keep a perfectly spherical framework) is placed at a distance L from the initial discontinuity, which is itself located $3L$ away from the sphere center, as illustrated by the sketch of Fig. 11

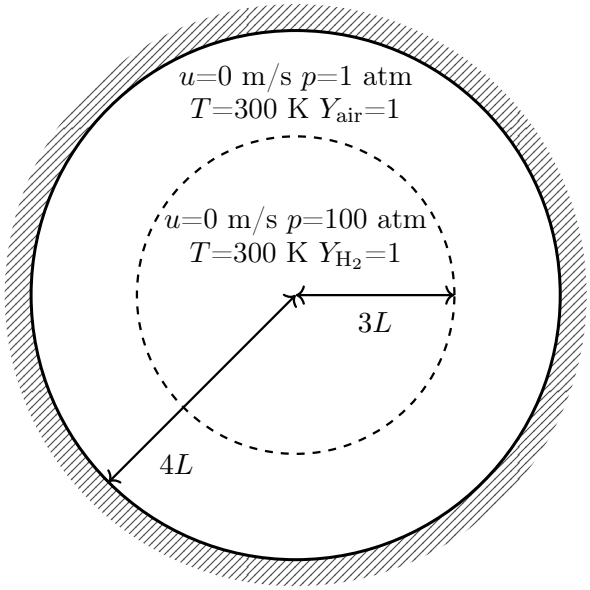

Figure 11: Sketch of the spherical shock test case.

Figure 12 illustrates the time evolution of the temperatures on the hydrogen side and on the air side for the spherical shock tube case presented earlier. The temperature obtained from the extrapolation on both sides of the contact is plotted in black as a reference. The regions where these curves are not plotted are due to a lack of points around the discontinuity, preventing a proper extrapolation. The diffusion layer hydrogen and air side temperature, computed using only the pressure evolution as developed for non-confined configurations, are shown in green while those computed using both the pressure evolution and the entropy jumps are displayed in red. Overall, the proposed methodology exhibits excellent agreement with the expected extrapolated values.

All the modifications are now validated and ready to be used for leakage in confined spaces.

3.6. Extended methodology

The final methodology used to determine whether a specific set of conditions (defined by $p_{\text{H}_2,0}$, r and L) leads to ignition of the high-pressure leakage is as follows:

- The initial shock tube problem is solved (H_2 at $p_{\text{H}_2,0}$ and air at atmospheric pressure) to obtain the two initial contact side temperatures

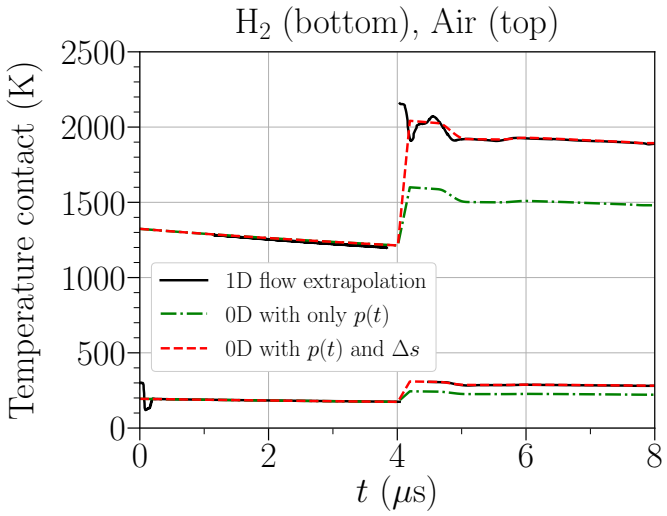

Figure 12: Time evolution of the temperature of the hydrogen and air side of the contact for the spherical shock problem: 1D flow extrapolation (black curve), diffusion layer pure hydrogen and air side values computed only from the time evolution of pressure (green dash-dotted curve) and from both the time evolution of pressure and entropy jump (red dashed curve).

$T_L(t{=}0)$ and $T_R(t{=}0)$, as well as the time t_E taken by the expansion wave to reach the centerline (see [2]).

- The pseudo-1D flow is simulated with the updated source term given by Eq. (14) or (15).
- At the shock-contact interaction time, t_{SC}, the states L_1 and S_1 are obtained from the flow extrapolation and used to recover the state R_1. The shock tube problem of the shock-contact interaction is then solved to obtain the states L_2 and R_2, and consequently the entropy jumps Δs_L and Δs_R.
- The diffusion layer is simulated normally with the pressure term $\frac{\mathrm{D}p}{\mathrm{D}t}$ until the shock-contact interaction, at which point the entropy jumps are applied to update the entire temperature profile using Eq. (23), after which the normal time integration is resumed.

4. Results

4.1. Effect of the confinement on the ignition process

This methodology can be applied first to observe the effects of the obstacle distance from the leakage L. Figure 13 shows the temporal evolution of the maximum OH mass fraction within the diffusion layer for three different wall distances: without the wall $\chi_L \to \infty$ (black curve), with the wall at a distance χ_L=12 (green dash-dotted curve), and with the wall at χ_L=11 (red dashed curve) for an initial hydrogen pressure of 65 atmosphere and a leakage size of 1 mm in 2D.

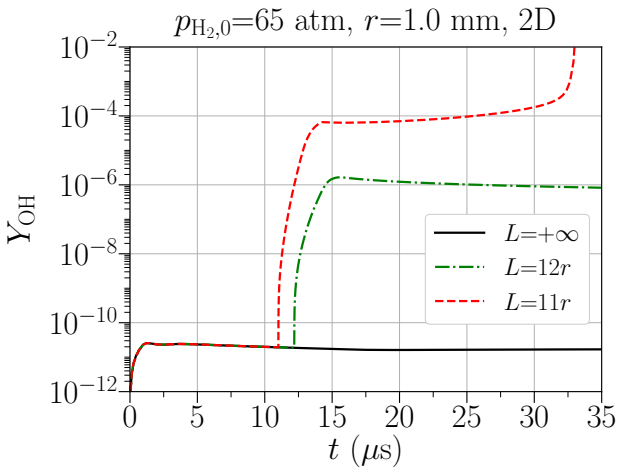

Figure 13: Time evolution of the maximum OH mass fraction within the diffusion layer for different wall positions ($p_{H_2,0}$=65 atm, r=1 mm).

In the absence of a wall, the OH mass fraction remains very low over time, showing that no ignition event occurs. When the wall positioned at a distance χ_L=12, the shock-contact interaction reactivates the chemistry; however, the ignition process is quenched shortly thereafter. The wall needs to be placed closer at χ_L=11 to achieve a complete ignition process after the interaction. This result shows that for a given set of hydrogen storage pressure and leakage size, a critical obstacle placement can be identified.

This test case also highlights that confinement can induce ignition at pressures significantly lower than those encountered in an open space. In the current confined configuration, the pressure is 65 atm, whereas no ignition was observed at pressures below 100 atm for the same case in an open environment in the previous study [2].

4.2. Effect of the confinement on the ignition limits

The effects of the confinement on the ignition limits for different geometries can be assessed. Figure 14 compares the ignition limits obtained for three geometries (3D tank in blue, 2D tank in red, and 2D pipe in green) for both an open-space leakage and a highly confined one, with the wall placed at χ_L =10.

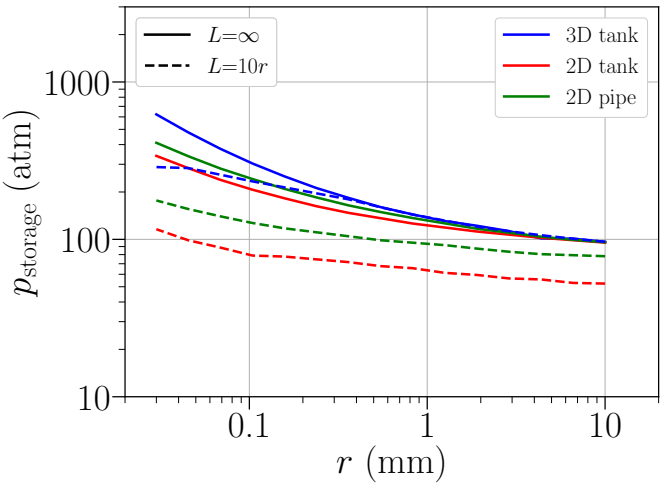

Figure 14: Comparison of the ignition limits obtained for different geometries (tank/pipe, 3D/2D) without and with the confinement effect of a wall placed at χ_L=10.

The main conclusion that can be drawn is the reduced effect of confinement for the 3D geometry compared to the 2D ones. The confinement effect in the 3D tank configuration becomes significant only for hydrogen storage pressures above 200 atm or leakage sizes below 0.3 mm, whereas it has a noticeable effect on 2D geometries across the entire range of conditions. This can easily be explained by the reduced expansion and weakening of the leading shock wave in two-dimensional geometries compared to their 3D counterparts. In 2D cases, the leading shock is much stronger when it reaches the obstacle and results in an even stronger reflected shock compared to 3D cases. This effect should not be neglected, as in a worst-case scenario, a hydrogen system with a pressure as low as 60 atm may be subject to spontaneous ignition if a large slit appears with an obstacle within 10 cm of the leakage, such as in an engine compartment.

Additionally, it should be noted that even in the case of a 2D pipe or 3D tank, the limit pressure for very small leakage sizes is still drastically reduced. While this simplified modeling approach may omit physical phenomena such

as wall friction and leakage opening time for small leakage sizes, the result nonetheless suggests a strong effect of the confinement on the ignition risk.

5. Conclusions

The impact of high-pressure hydrogen leakage in confined spaces, as opposed to open environments, was thoroughly examined by adapting the methodology introduced in a previous study. The modifications allowed for accurate flow reconstruction along the centerline, including shock-contact interactions, while an extrapolation method was employed to analytically determine the resulting states. These predicted states were then used to derive entropy jumps, updating the diffusion layer temperature profile to account for the non-isentropic nature of the interaction.

The findings indicate that confinement has a significant effect on two-dimensional leakage under all conditions, whereas its influence on three-dimensional leakage is limited to cases of high pressure or small leakage sizes. These insights not only improve our understanding of hydrogen ignition risks in confined environments but also provide valuable input for the development of safety standards for hydrogen storage systems.

Nevertheless, it is important to acknowledge that the present modeling approach is based on an idealized configuration, where the shock wave surfaces are assumed to be perfectly smooth. In real-world scenarios, however, reflected shocks are likely to exhibit strong perturbations, for example due to non-uniformities in the confining walls, leading to wrinkled shock interfaces and the formation of multiple triple points. These effects may considerably alter the ignition dynamics compared to the simplified setup considered here.

Furthermore, leakage opening dynamics constitute another limitation of the present work, as they can strongly influence the development of the leading shock wave and, consequently, the ignition risk in both open and confined environments. This point is key and could be addressed in future work to improve the relevance of the present approach to real applications for both open and confined leakage.

6. Acknowledgments

Part of this research was supported by the French project BALBUZARD funded by DGAC and supported by Next generation EU in the frame of "Plan national de Relance et de Résilience français (PNRR)" ; and by the ANR, Airbus, Fives-Pillard and SafranTech through the Industrial Chair Program LIBERTY ANR-23-CHIN-0005.

References

[1] P. Boivin, M. Le Boursicaud, A. Millán-Merino, S. Taileb, J. Melguizo-Gavilanes, F. A. Williams, Hydrogen ignition and safety, in: Hydrogen for Future Thermal Engines, Springer, 2023, pp. 161–236.

[2] M. Le Boursicaud, S. Zhao, J.-L. Consalvi, P. Boivin, A reduced order numerical model for high-pressure hydrogen leak self-ignition, Combust. Flame 274 (2025) 114003.

[3] B. Maxwell, M. Radulescu, Ignition limits of rapidly expanding diffusion layers: Application to unsteady hydrogen jets, Combust. Flame 158 (2011) 1946–1959.

[4] V. Mironov, O. Penyazkov, D. Ignatenko, Self-ignition and explosion of a 13-mpa pressurized unsteady hydrogen jet under atmospheric conditions, Int. J. Hydrog. Energy 40 (2015) 5749–5762.

[5] P. Li, Q. Duan, K. Jin, Q. Zeng, J. Sun, Experimental study on shock waves, spontaneous ignition, and flame propagation produced by pressurized hydrogen release through tubes with varying obstacle location, Fuel 290 (2021) 120093.

[6] X. Pan, Q. Zhang, Y. Jiang, M. Hua, Z. Wang, J. Jiang, Effects of circular obstacle size on shock wave and spontaneous ignition following sudden release of pressurized hydrogen, J. Energy Storage 116 (2025) 116124.

[7] A. Smygalina, A. Kiverin, Self-ignition of hydrogen jet due to interaction with obstacle in the obstructed space, Int. J. Hydrog. Energy 47 (2022) 35877–35885.

[8] B. Xu, J. X. Wen, V. Tam, The effect of an obstacle plate on the spontaneous ignition in pressurized hydrogen release: A numerical study, Int. J. Hydrog. Energy 36 (2011) 2637–2644.

[9] K. Schmidmayer, F. Petitpas, S. Le Martelot, É. Daniel, Ecogen: An open-source tool for multiphase, compressible, multiphysics flows, Comput. Phys. Commun. 251 (2020) 107093.

[10] M. Le Boursicaud, S. Zhao, J.-L. Consalvi, P. Boivin, An improved passive scalar model for hydrogen hazardous ignition prediction, Combust. Flame 256 (2023) 112938.

[11] P. L. Roe, Some contributions to the modelling of discontinuous flows, in: Large-scale computations in fluid mechanics; Proceedings of the Fifteenth Summer Seminar on Applied Mathematics, 1985, pp. 163–193.

[12] A. Chiapolino, R. Saurel, B. Nkonga, Sharpening diffuse interfaces with compressible fluids on unstructured meshes, J. Comput. Phys. 340 (2017) 389–417.

[13] E. F. Toro, Riemann solvers and numerical methods for fluid dynamics: a practical introduction, Springer Science & Business Media, 2013.

Appendix A. Extrapolation procedure validation

1D planar

The choice of indices used to fit the polynomials can be easily validated with a shock tube problem involving a wall. The first test case is purely 1D, with hydrogen at 100 atm on the left side and air at atmospheric pressure on the right side, both initially at 300 K, with an obstacle placed at a distance L from the initial discontinuity. Figure A.15 presents the density profile around the shock-contact interaction. The exact solution is shown as a solid blue line while the solution obtained by the flow solver is depicted with a dashed black line with the corresponding computational cells being identified with black circles. The diagrams on the left shows solutions obtained using a coarse mesh ($L/\Delta x$=400) while the one on the right uses a finer mesh ($L/\Delta x$=600). The use of two different mesh sizes is intended to highlight the independence of the number of cells over which the waves are numerically thickened, supporting the choice to maintain a constant number of cells between the wave "center" and the points used for extrapolation. The cells used to construct the polynomials are highlighted with red and green cross markers on the right and left sides, respectively, and the corresponding extrapolated polynomials are represented by red and green dashed lines.

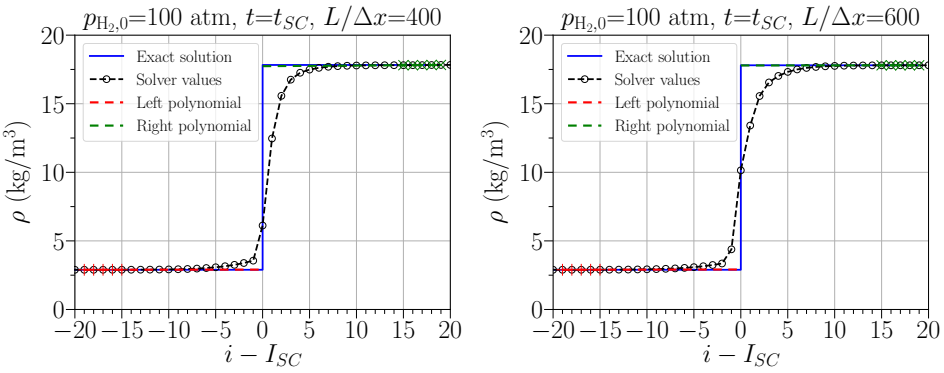

Figure A.15: Density profile for an initial hydrogen pressure $p_{H_2,0}$ =100 atm, at a time $t = t_{SC}$ zoomed on the cells around the interaction. The exact solution (blue line), flow solver solution (black dashed line) with the actual cells marked by open circles are plotted for a coarse mesh (left diagram) and a fine mesh (right diagram). On each diagram, the left and right cells used to fit the polynomials are highlighted by red and green cross markers, respectively, and the resulting extrapolated polynomials are represented by dashed lines.

Figure A.15 shows that, as expected, the numerical thickening is identical for both grid resolutions. The polynomial extrapolations predict the correct

value at the interface. These results show that the choice of 15 cells between the contact and the values used for the fitting is sufficient. This is confirmed in Fig. A.16 which considers a higher initial pressure of $p_{H_2,0} = 300$ atm.

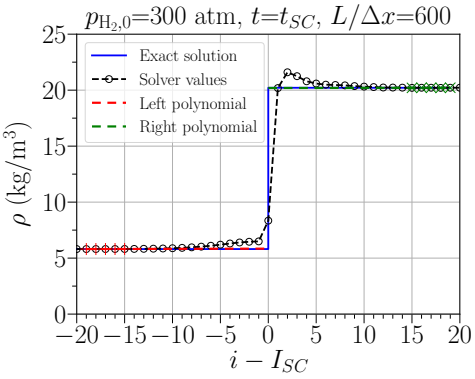

Figure A.16: Density profile for an initial hydrogen pressure $p_{H_2,0} = 300$ atm, at a time $t = t_{SC}$ zoomed on the cells around the interaction. The exact solution is represented by a blue line and the flow solver solution by a black dashed line with the actual cells marked by open circles. The left and right cells used to fit the polynomials are highlighted by red and green cross markers and the resulting extrapolated polynomials are represented by dashed lines.

This test case is the first step in validating the extrapolation method; however, further testing is required for more representative cases.

1D spherical

To validate the extrapolation strategy for more complex flow topologies, the spherical shock reflection test case presented in Sec. 3.5 is used. It consists of a shock tube in spherical coordinates, with hydrogen at 100 or 300 atm on the left side and air at atmospheric pressure on the right, both initially at 300 K. An obstacle is placed at a distance L from the initial discontinuity, which is itself located $3L$ away from the sphere center.

No analytical solution is available for this test case. Figure A.17 shows the density profiles obtained with the pseudo-1D (using the appropriate source term $\mathcal{S}(x,t) = 2/x$ [2, 13]) solver for two initial pressures of 100 atm (left) and 300 atm (right). The left and right cells used for the fitting are highlighted by red and green crosses and the resulting polynomials are represented by red and green dashed lines, respectively. These results show clearly that polynomials need to be first-order. The accuracy of the methodology is further demonstrated as a perfect reconstruction of the flow around the discontinuities is obtained.

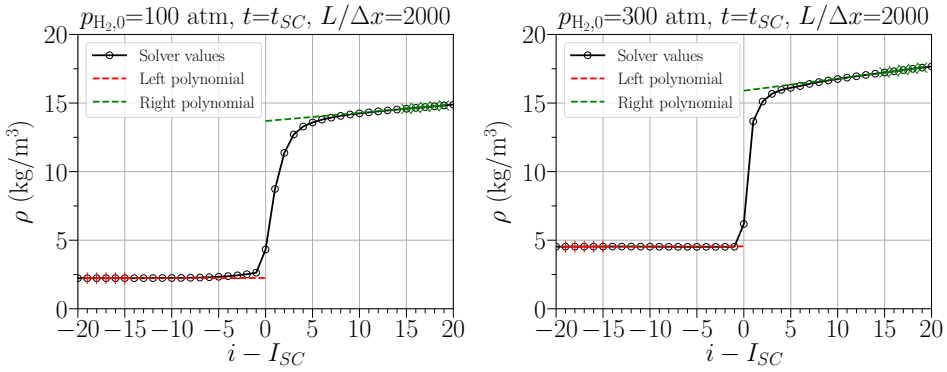

Figure A.17: Density profile for the spherical shock tube problem with an initial hydrogen pressure $p_{H_2,0}$=100 atm (left) and $p_{H_2,0}$=300 atm (right), at a time t=t_{SC} zoomed on the cells around the interaction. The flow solver solution is represented by a black line with the actual cells marked by open circles. The left and right cells used to fit the polynomials are highlighted by red and green cross markers and the resulting extrapolated polynomials are represented by dashed lines.

In addition to the density extrapolation, Fig. A.18 shows the velocity and pressure extrapolations for the spherical case at $p_{H_2,0}$=100 atm. This validates the present method, which is perfectly suited to reconstruct both sides of the shock-contact interaction without introducing numerical artifacts.

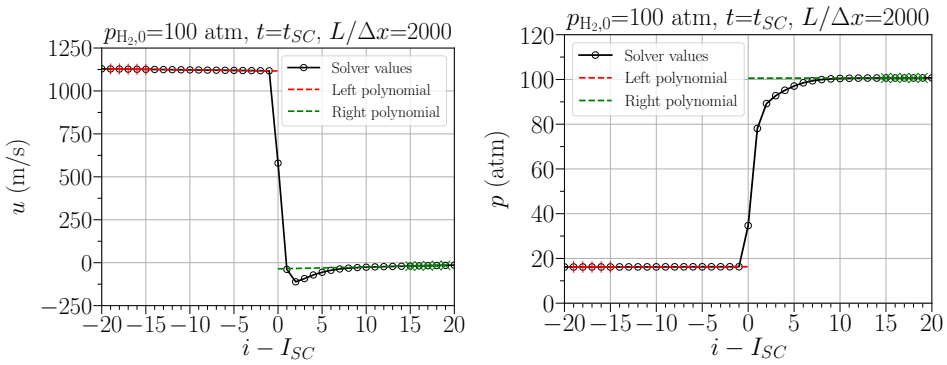

Figure A.18: Velocity (left) and pressure (right) profiles for the spherical shock tube problem with an initial hydrogen pressure $p_{H_2,0}$=100 atm, at a time t=t_{SC} zoomed on the cells around the interaction. The flow solver solution is represented by a black line with the actual cells marked by open circles. The left and right cells used to fit the polynomials are highlighted by red and green cross markers and the resulting extrapolated polynomials are represented by dashed lines.